

# Time-resolved SAXS characterization of the shell growth of silica-coated magnetite nanocomposites

Alexander Gutsche · Alexander Daikeler ·  
Xiaoai Guo · Nico Dingenouts · Hermann Nirschl

Received: 3 February 2014 / Accepted: 20 May 2014 / Published online: 6 June 2014  
© Springer Science+Business Media Dordrecht 2014

**Abstract** Time-resolved characterization of silica-coated magnetite nanoparticles during synthesis is performed using our self-developed small-angle X-ray scattering (SAXS) instrument. The shell growth (5–20 nm) is determined quantitatively using a core-shell sphere model. SAXS analyses provide reliable information on the shell thickness despite the complex geometry of the synthesized nanocomposites. They are in good agreement with transmission electron microscope (TEM) observations. Firstly, time-resolved SAXS analyses are used to study the influence of the precursor concentration (tetraethyl orthosilicate) on growth kinetics. Time evolution of the shell thickness can be described by diffusion-limited shell growth, obeying kinetics of first order in the precursor concentration. Furthermore, SAXS measurements provide information on the standard deviation of the shell thickness as a function of the coating time. Its decrease

observed with increasing coating time is explained by a self-sharpening mechanism and/or a morphology evolution to more isometric shapes. Additionally, the influence of ammonia is studied. By increasing its concentration, the growth rate is affected. However, the final shell thickness and the standard deviation do not change significantly. For low ammonia concentration, by contrast, the SAXS and TEM observations reveal superimposed silica gelation. In addition, coating reaction was conducted at elevated temperature (40 °C). SAXS patterns measured as a function of the coating time and TEM micrographs reveal simultaneous production of classic Stöber particles under these conditions. Hence, SAXS is found to have a big potential for on-line monitoring of the shell properties.

**Keywords** Small-angle X-ray scattering · Silica-coated magnetite · Growth kinetics · On-line monitoring

**Electronic supplementary material** The online version of this article (doi:10.1007/s11051-014-2475-2) contains supplementary material, which is available to authorized users.

A. Gutsche (✉) · A. Daikeler · X. Guo · H. Nirschl  
Institute for Mechanical Process Engineering and  
Mechanics, Karlsruhe Institute of Technology, Strasse am  
Forum 8, 76131 Karlsruhe, Germany  
e-mail: alexander.gutsche@kit.edu

N. Dingenouts  
Institute for Technical Chemistry and Polymer Chemistry,  
Karlsruhe Institute of Technology, Engesserstrasse 18,  
76131 Karlsruhe, Germany

## Introduction

In recent years, magnetic nanoparticles attracted increasing attention of many researchers. As the most common representative of magnetic nanoparticles, magnetite  $\text{Fe}_3\text{O}_4$  was investigated extensively in the past decade. The  $\text{Fe}_3\text{O}_4$  particles exhibit superparamagnetic properties, if the particle size is less than the magnetic domain. By applying an external magnetic

field, the particles can reach a considerable magnetization (Jeong et al. 2007). When removing the external field, however, remanent magnetization becomes zero. Once properly designed and functionalized,  $\text{Fe}_3\text{O}_4$  particles have a great potential in many applications, e.g., in medicine and in bioscience, for magnetic bioseparation and magnetic resonance imaging (MRI) (Jeong et al. 2007; Shinkai 2002; Safarik and Safarikova 2002; Elingarami and Zeng 2011; Hasany et al. 2013). Strong magnetic dipolar interactions, however, easily result in agglomeration. Consequently,  $\text{Fe}_3\text{O}_4$  clusters have a low dispersibility in aqueous media, which is disadvantageous for many applications. Furthermore,  $\text{Fe}_3\text{O}_4$  tends to oxidize, causing reduced magnetization. To overcome the problems of colloidal and chemical instability, the  $\text{Fe}_3\text{O}_4$  particles can be coated by a compact silica shell using various synthesis methods, e.g., by microemulsions, hydrolysis of iron sulfate, and deposition from silicic acids (Ding et al. 2012; Bruce et al. 2004). The most prominent route for the production of silica-coated magnetic nanoparticles ( $\text{Fe}_3\text{O}_4@\text{SiO}_2$ ) is the sol-gel method according to Stöber et al. (1968). In this method, tetraethyl orthosilicate (TEOS) is hydrolyzed, followed by condensation. Besides the stabilizing effect, the silica surface provides many hydroxyl groups for various types of functionalization for further applications. Furthermore, it is known that the properties of  $\text{Fe}_3\text{O}_4@\text{SiO}_2$  particles are strongly affected by the mean shell thickness (Liu et al. 2008). As shown by Caruana et al. (2012), the magnetic saturation decreases significantly after coating magnetic particles with a compact silica shell. To achieve sufficient magnetization, the shell thickness must not exceed a critical maximum. On the other hand, too thin silica shells do not provide for a sufficient colloidal stability, resulting in aggregation (Philipse et al. 1994). It is therefore of crucial importance to control the coating process with regard to the resulting shell thickness.

Mostly, transmission electron microscopy (TEM) was used for off-line and ex-situ determination of the mean shell thickness of final products (Caruana et al. 2012; Deng et al. 2005; Mine et al. 2003). However, time-resolved characterization is often required to control the product quality on-line, i.e., to avoid undesired inhomogeneities like high shell thickness polydispersity or inhomogeneity due to co-existing homogeneous silica and highly agglomerated

morphology. Thanks to the short measurement time, small-angle X-ray scattering (SAXS) is a promising and frequently used measurement technique for time-resolved studies of particle properties. Furthermore, the particles can be analyzed in situ, i.e., the characterization can be conducted under reaction conditions (Boukari et al. 1997a, b; Pontoni et al. 2002; Tobler and Benning 2013). In this way, secondary effects during sample preparation, e.g., aging, nucleation, and aggregation, can be prevented. Another advantage is associated with the non-destructive nature of the soft X-rays used for SAXS analysis. Due to the inverse characteristics of the measured scattering intensities, however, data treatment often requires complex approaches (e.g., inverse Fourier transform, fitting of correlation functions) to obtain information on structural properties. Theoretical scattering intensity profiles can be computed for many three-axial bodies, examples can be found in the literature (Guinier and Fournet 1955; Glatter and Kratky 1982). Using a proper theoretical model, it is possible to extract reasonable approximations of structural parameters of interest, e.g., particle size and shape.

Numerous papers demonstrate how information on particle properties can be obtained by means of SAXS. Besides investigations of fractal structures (Beaucage 1996; Wengeler et al. 2007; Boukari et al. 1997a), SAXS is often used for the determination of the particle size, as done by Pontoni et al. (2002), who carried out SAXS measurements to investigate the nucleation and growth processes of colloidal silica particles. For many particle systems, a hard sphere model is used for fitting the experimental data. Often, however, more complex structures are of interest. For instance, Chen et al. (2013) performed SAXS studies of hollow nanoparticles using a hollow triple-shell ellipsoidal model. On this basis, the radii of the outer and inner shells and the axial ratio were extracted. Another study deals with the kinetics of droplets in oil-in-water emulsions (Roshan Deen et al. 2009). The droplet size determined by SAXS was in good agreement with the time-resolved turbidity measurements. This confirmed the usefulness of SAXS.

Mostly, synchrotron radiation is required for the investigation of complex particle systems. In fact, the synchrotron is a powerful measurement device for structure analysis. However, the portable laboratory-scale SAXS instrument can be used more flexibly in laboratories, which often is required. Recently, use of

our self-developed laboratory-scale SAXS device for time-resolved investigations of the synthesis of specific multiplet-like silica particles was reported (Gortz et al. 2012). By means of theoretical intensity profiles, the so-called non-isometry ratio was deduced to specify the multiplet's shape.

To the best of our knowledge, there have not yet been any reports dealing with the investigation of the shell growth dynamics of  $\text{Fe}_3\text{O}_4@\text{SiO}_2$  composites by SAXS. This work therefore demonstrates how time-resolved observations of the shell growth can be conducted by means of a laboratory-scale SAXS device. To this end, magnetic particles were synthesized by co-precipitation and coated with silica according to Stöber process under various coating conditions. Time-resolved SAXS measurements allow conclusions to be drawn with respect to the growth kinetics. Furthermore, the high potential for on-line monitoring of the particle properties by means of SAXS is demonstrated.

## Experimental

### Materials

For the synthesis of  $\text{Fe}_3\text{O}_4$ , iron(II) chloride tetrahydrate was purchased from Merck (Germany), and iron(III) chloride hexahydrate was purchased from Alfa Aesar (USA). For the stabilization of  $\text{Fe}_3\text{O}_4$ , trisodium citrate dihydrate was purchased from VWR BDH Prolabo (Germany). Ammonia (for analyses) used for both the synthesis of  $\text{Fe}_3\text{O}_4$  and the coating by silica was purchased from APPLICHEM (Germany). The silica coating was accomplished using TEOS (for syntheses) purchased from Merck (Germany). For all experiments, ultrapure water prepared using the device arium<sup>®</sup> pro (Sartorius, Germany) was used.

### *Fe<sub>3</sub>O<sub>4</sub> synthesis and its preparation for silica coating*

$\text{Fe}_3\text{O}_4$  synthesis was carried out by the co-precipitation of  $\text{FeCl}_3$  and  $\text{FeCl}_2$  in alkaline media, as was firstly described by Massart (1981). Following the procedure described by Zhang et al. (2011), 250 mL of 0.7 M ammonia solution was stirred rigorously in a three-neck flask. Then, a mixture of 20 mL iron(III) chloride (1 M in ultrapure water) and 5 mL iron(II) chloride (2 M in 2 M hydrochloric acid) was added in a

dropwise manner to the ammonia solution, directly followed by the formation of a black precipitate. After 30 min of rigorous stirring, the suspension was filled into a beaker. The precipitate was separated by means of a permanent magnet and washed by ultrapure water. This procedure was repeated at least four times. Then, the particles were stabilized by dissolving the black precipitate in 200 mL 0.5 M trisodium citrate solution under ultrasound treatment. After that, the stabilized suspension was stirred overnight in order to ensure sufficient adsorption of citrate ions on the particle surface for efficient stabilization. However, as was predicted by the DLVO theory, excess citrate ions may have a destabilizing effect on the particles. Therefore, the excess citrate ions had to be removed by further washing. According to Zhang et al. (2011), this can be done by the use of ethanol as a washing liquid. In this way, efficient particle deposition is achieved, which helps to prevent high product losses in the supernatant phase. The quick sedimentation of  $\text{Fe}_3\text{O}_4$  in ethanol is promoted by agglomeration which can be explained by reduced repulsion due to a low dielectric constant of ethanol as compared to water (Gregory et al. 2009). However, the stabilized and washed suspension turned out to agglomerate and sediment after the  $\text{Fe}_3\text{O}_4$  solution had been fed into the flask for the following coating procedure. In case of untreated  $\text{Fe}_3\text{O}_4$  solution, by contrast, no sedimentation problems were observed. Due to the insolubility of trisodium citrate in ethanol, the excess ions probably had not been removed efficiently enough. Hence, washing was accomplished using ethanol, followed using water in the last washing step. The  $\text{Fe}_3\text{O}_4$  solutions prepared in this way were stable and did not show any precipitation problems.

### *Synthesis of Fe<sub>3</sub>O<sub>4</sub>@SiO<sub>2</sub>*

The mass concentration of the synthesized and stabilized  $\text{Fe}_3\text{O}_4$  was adjusted to 30 mg/mL for subsequent silica coating using the sol-gel method (Stöber et al. 1968). Firstly, ethanol (23 g), ultrapure water (80 g), ammonia (3.6 g, 25 % m/m), and 4 mL of the prepared  $\text{Fe}_3\text{O}_4$  suspension were fed into a three-neck flask. This mixture was subjected to an ultrasonic treatment for 20 min to achieve homogeneous dispersion. Then, a defined amount of TEOS was added to the flask in drops under rigorous stirring. Except for the sample T043N13-40 (Table 1), all experiments were conducted at ambient temperature.

**Table 1** Initial reaction conditions

Sample name	$c_{\text{TEOS}}$ (mol/L)	$c_{\text{NH}_3}$ (mol/L)	$c_{\text{EtOH}}$ (mol/L)
$T_r = 20\text{ }^\circ\text{C}$			
T017N13-20	0.017	0.13	13.27
T026N13-20	0.026	0.13	13.25
T035N13-20	0.035	0.13	13.22
T043N13-20	0.043	0.13	13.20
T052N13-20	0.052	0.13	13.17
T035N06-20	0.035	0.06	13.20
T035N39-20	0.035	0.39	13.18
$T_r = 40\text{ }^\circ\text{C}$			
T043N13-40	0.043	0.13	13.18

### Characterization methods

TEM analyses were conducted with a Philips CM12 device at 120 kV. The TEM micrographs were analyzed using ImageJ. The mean shell thickness was determined by averaging at least 150 values. The Stokes diameter of  $\text{Fe}_3\text{O}_4$  agglomerates was determined using an analytical ultra-centrifuge (AUC). SAXS analyses were carried out with a modified Kratky camera. The incident beam was monochromated ( $\lambda = 0.154\text{ nm}$ ) and focused on the detection plane by means of a Goebel mirror. A two-dimensional imaging plate detector was used for the detection of the scattering intensity as a function of the scattering angle. Due to the slit beam geometry, the raw data had to be desmeared after background subtraction. More detailed information on the SAXS instrument can be found elsewhere (Goertz et al. 2009, 2012; Guo et al. 2013a, b).

Determination of the mean shell thickness from SAXS data

Core-shell nanocomposites were characterized using the laboratory-scale SAXS instrument described above. The short measurement time of 3 min allows for time-resolved data acquisition during progressing coating reaction. Data evaluation is based on a spherical core-shell model, including polydispersity. The scattering intensity of monodisperse core-shell spheres  $I_0$  as a function of the modulus of the scattering vector  $q = \frac{4\pi}{\lambda} \sin(\theta)$ , where  $\theta$  denotes the

half scattering angle, can be calculated by squaring the scattering amplitude  $A_{\text{cs}}(q)$ :

$$I_0(q) = |A_{\text{cs}}(q)|^2. \quad (1)$$

The amplitude of a core-shell sphere is given by the equation

$$A_{\text{cs}}(q) = \Delta\rho_s V_{\text{total}} \Phi(qr_s) + (\Delta\rho_c - \Delta\rho_s) V_c \Phi(qr_c), \quad (2)$$

$V_{\text{total}}$  and  $V_c$  stand for the total particle volume and the core volume, respectively.  $\Delta\rho_c = \rho_c - \rho_{\text{solv}}$  and  $\Delta\rho_s = \rho_s - \rho_{\text{solv}}$  denote the excess electron density of the core with the electron density  $\rho_c$  and the shell with the electron density  $\rho_s$ , respectively. The electron density of the surrounding solvent is denoted by  $\rho_{\text{solv}}$ . In this work, the electron densities are set to  $\rho_c = \rho_{\text{Fe}_3\text{O}_4} = 1.49 \times 10^{24}\text{ cm}^{-3}$ ,  $\rho_s = \rho_{\text{SiO}_2} = 6.62 \times 10^{23}\text{ cm}^{-3}$ , and  $\rho_{\text{solv}} = \rho_{\text{H}_2\text{O}} = 3.34 \times 10^{23}\text{ cm}^{-3}$ . The function  $\Phi(qr)$  is defined as follows:

$$\Phi(qr) = 3 \frac{\sin(qr) - qr \cos(qr)}{(qr)^3}. \quad (3)$$

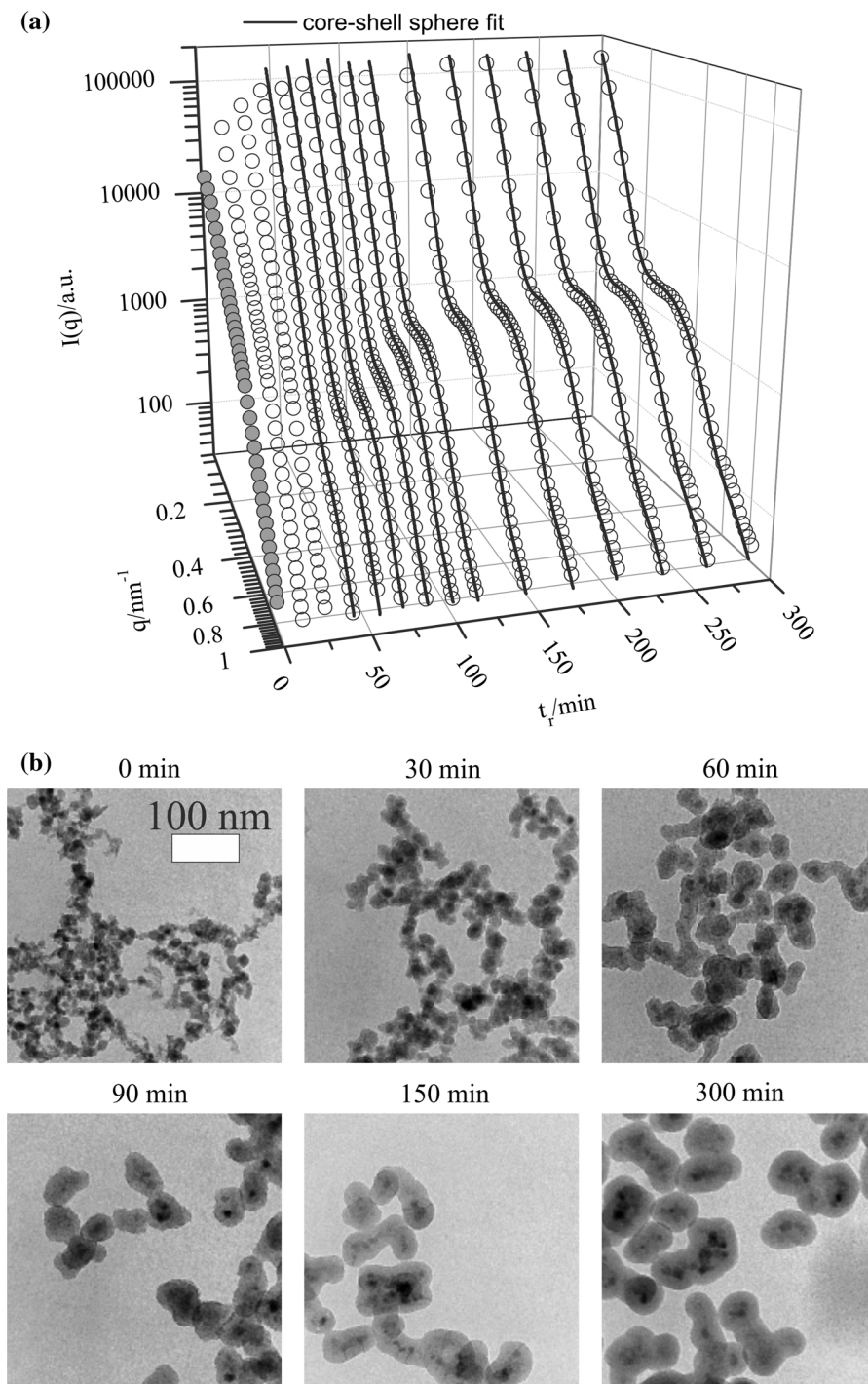
Assuming constant electron densities, the scattering amplitude only depends on the core and shell radius  $r_c$  and  $r_s$ , respectively. Since real particle systems mostly exhibit polydispersity, Eq. 1 has to be extended to:

$$I(q) = \sum_{i=1}^n \sum_{j=1}^m \left[ G_c(r_c^{(i)}) G_s(r_s^{(j)}) |A_{\text{cs}}(q, r_c^{(i)}, r_s^{(j)})|^2 \right], \quad (4)$$

$G_c(r_c^{(i)})$  and  $G_s(r_s^{(j)})$  are distributions of the core and shell radius, respectively (in this work the log-normal distribution was chosen, and the standard deviation of the core and the shell is denoted by  $\sigma_c$  and  $\sigma_s$ , respectively). In general, it is known that the SAXS curve will exhibit pronounced side maxima, if the shell is not too polydisperse. Furthermore, it is known from theoretical calculations using Eq. 4 that the side maxima will not be affected significantly by varying the core-related parameters  $r_c$  and  $\sigma_c$ . Thus,  $r_c$  and  $\sigma_c$  can be set to arbitrary values (e.g.,  $r_c = 50\text{ nm}$  and  $\sigma_c = 50\%$ ), and Eq. 4 yields the shell-related parameters of interest  $r_s$  and  $\sigma_s$ . Exemplary calculations of theoretical SAXS curves using Eq. 4 can be found in the supplementary materials (Fig. S1).

In this study,  $\text{Fe}_3\text{O}_4$  particles were synthesized by co-precipitation and served as core particles for the following

**Fig. 1** SAXS results and TEM micrographs of particles for  $c_{\text{TEOS}} = 0.026$  mol/L. **a** Measured scattering curves  $I(q)$  versus reaction time  $t_r$  and fitted by the core-shell sphere model (Eq. 4); **b** TEM micrographs at variable  $t_r$ , the scale bars are 100 nm in all images



coating process. As depicted by Fig. 1a, the scattering curve of the pure  $\text{Fe}_3\text{O}_4$  (grey circle) does not show any side maxima, which indicates polydispersity and irregular particle morphology. However, the used sphere

model implies that the core is composed of an ideal sphere with a radius  $r_c$ . To take into account, complex core morphology (e.g., fractal agglomerates), only numerical methods, e.g., the finite elements approach, can be used

(Debye 1915). In fact, this would allow for more realistic modeling. In case of core–shell composites, the numerical effort is enormous. The computing time is determined mainly by the reciprocal distances of the finite elements and by the computation of  $\sin x/x$  terms. Assuming a spherical composite composed of a core with radius  $r_c = 25$  nm and a shell with the thickness  $T_s = 10$  nm ( $T_s = r_s - r_c$ ), the number of  $\sin x/x$  computations can be assessed to be in the order of  $10^{14}$ . To ensure sufficient accuracy, a  $q$ -range of  $0.01 \dots 2 \text{ nm}^{-1}$  with a resolution  $\Delta q = 0.01 \text{ nm}^{-1}$  and a ratio  $T_s/r_c = 40$  ( $r_c$  denotes the radius of a spherical finite element) were chosen (Goertz et al. 2012; Glatter and Kratky 1982). As a consequence of the large number of finite elements, this approach would require a practically unfeasible computing time. The simplifying assumption of spherical geometry, by contrast, allows for an analytical computation of scattering intensities, where only polydispersity has to be approximated numerically by Eq. 4.

## Results and discussion

### Dynamics of shell growth for various initial TEOS concentrations

The coating of  $\text{Fe}_3\text{O}_4$  using the classic Stöber method was investigated by time-resolved SAXS measurements and TEM analyses. The reaction conditions are summarized in Table 1. Firstly, the initial TEOS concentration  $c_{\text{TEOS}}$  was varied between 0.017 and 0.052 mol/L. The concentrations of ammonia and ethanol were fixed to  $c_{\text{NH}_3} = 0.13$  mol/L and  $c_{\text{EtOH}} = 13.25$  mol/L, respectively. Figure 1a exemplarily shows the scattering curves  $I(q)$  measured for  $c_{\text{TEOS}} = 0.026$  mol/L (T026N13-20, Table 1) at variable reaction times  $t_r$ . Before the coating reaction was initiated, the measured SAXS curve did not show any specific side maxima (grey circle, Fig. 1a), indicating high polydispersity and irregular morphology of the naked  $\text{Fe}_3\text{O}_4$  particles. In fact, the product appeared to have the form of agglomerated primary particles as was shown by TEM micrographs in Fig. 1b for  $t_r = 0$  min. This was due to the fast particle formation kinetics in case of co-precipitation and the high inter-particulate dipolar magnetic forces. Measurements by AUC revealed a Stokes diameter of the agglomerates of  $d_{\text{agg,AUC}} = 39.8 \pm 1.1$  nm.

As TEOS was introduced, a thin silica shell was formed on the surface of the  $\text{Fe}_3\text{O}_4$  particles by heterogeneous nucleation. As a consequence, the scattering intensity at small  $q$  increased (Fig. 1a). After  $t_r = 45$  min, a side maximum was observed at large  $q$ , which can be attributed to scattering by the formed silica shell. TEM micrographs in Fig. 1b clearly demonstrate that a visible silica shell has already been formed on the surface of the  $\text{Fe}_3\text{O}_4$  particles after a period of 30 min and becomes thicker while the reaction progresses. For quantitative determination of  $T_s$  as a function of  $t_r$ , the measured SAXS profiles were fitted by Eq. 4 using the core–shell sphere model (Fig. 1a, solid lines). Obviously, the side maximum of the scattering curves can be described properly by Eq. 4. Figure 2a illustrates the resulting shell thicknesses as a function of the coating time for variable  $c_{\text{TEOS}}$ . As can be seen, the final shell thicknesses were reached after a period of about 360 min. As expected, the higher TEOS concentration was adjusted, the thicker the final shell thickness was, i.e., by adjusting the appropriate precursor concentration, the final shell thickness can be controlled. Figure 2b shows the final  $T_s$  provided by SAXS (black circle) and TEM (times) plotted versus  $c_{\text{TEOS}}$ . Interestingly, the SAXS results are in good agreement with the TEM observations despite the irregular morphology of the synthesized composites. The slight underestimation of SAXS results may be caused by the real particle shape, which deviates from the assumed ideal core–shell sphere. On the other hand, it is always difficult to determine correct shell thicknesses from TEM, and a large amount of particles is required to produce reliable values. For non-isometric particles, the thickness has to be determined for several orientations of the particle. In addition, the contrast of the phases may influence the shell thickness seen in TEM examinations.

Since SAXS measurements provide time-resolved information on the shell thickness, the growth rate can be calculated easily. According to Sugimoto (1987), the growth rate will decrease with increasing particle size  $r$ , if the reaction kinetics is assumed to be of first order in monomer concentration, and the particle growth is limited by diffusion of monomers. In this case, the growth rate obeys the relation  $\Delta r/\Delta t \sim A(r^{-1} + B)$ . The parameter  $A$  depends on the diffusion coefficient, molecular weight, and the bulk concentration of the monomers, and  $B$  denotes the reciprocal of the

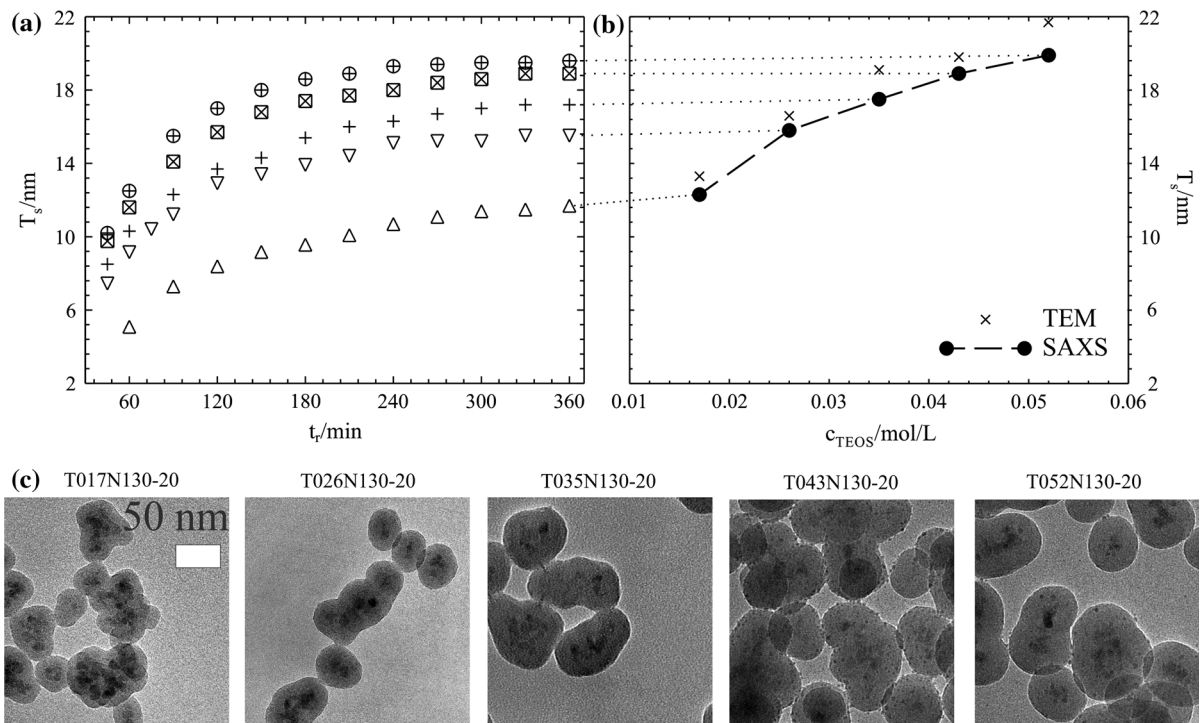


**Fig. 2** **a** Shell thickness  $T_s$  measured by SAXS versus the reaction time  $t_r$  for  $c_{TEOS} = 0.017$  mol/L (white up-pointing triangle),  $c_{TEOS} = 0.026$  mol/L (white down-pointing triangle),  $c_{TEOS} = 0.035$  mol/L (plus),  $c_{TEOS} = 0.043$  mol/L (squared

times),  $c_{TEOS} = 0.052$  mol/L (circled plus); **b** the final shell thickness measured by SAXS (black circle) and TEM (times); **c** TEM micrographs of final products, the scale bars are 50 nm in all images

diffusion layer thickness. Figure 3 depicts the shell growth rate  $\Delta T_s / \Delta t_r$  versus  $T_s$ , obtained from the time-resolved data shown in Fig. 2a. The lines represent the growth rate dependency for the case of diffusion-limited particle growth. Obviously, the growth rates are affected by the initial  $c_{TEOS}$ , i.e., the higher the initial  $c_{TEOS}$  was adjusted, the higher was the resulting growth rate.

Moreover, as a consequence of diffusion-limited growth, the standard deviation is expected to decrease with increasing shell thickness (self-sharpening mechanism) (Sugimoto 1987). In fact, the standard deviations  $\sigma_s$  measured by SAXS support the suggested self-sharpening with increasing coating time (see Fig. 4). For the sake of clarity, the standard deviations are shown separately in Fig. 4a for  $c_{TEOS} = 0.017$  mol/L (white up-pointing triangle)  $c_{TEOS} = 0.026$  mol/L (white down-pointing triangle) and  $c_{TEOS} = 0.035$  mol/L (plus) and in Fig. 4b for  $c_{TEOS} = 0.043$  mol/L (squared times) and  $c_{TEOS} = 0.052$  mol/L (circled plus). Obviously, the graphs show a large standard deviation at the beginning of the coating process for all

$c_{TEOS}$  which significantly decreases with increasing  $t_r$ . Apart from the self-sharpening mechanism,  $\sigma_s$  may also be affected significantly for other reasons, e.g., non-spherical particle shape. It is known that SAXS curves of ideal core-shell spheres exhibit the most pronounced side maxima due to the isometric geometry. In other words, the scattering curves become less pronounced with increasing deviation from the ideal sphere. As a consequence of the additional structure loss in the profiles, Eq. 4 will provide overestimated values for  $\sigma_s$  in case of non-isometric bodies. From the TEM micrographs in Fig. 1b, it is obvious that particle morphology developed from highly branched agglomerates at the beginning of the reaction to more isolated unbranched composites at the end of the coating reaction. Consequently, a more isotropic geometry may result, which may explain the decrease of  $\sigma_s$  with  $t_r$ .

Furthermore,  $\sigma_s$  approaches a steady state in case of low  $c_{TEOS}$  (Fig. 4a). At higher  $c_{TEOS}$ , the standard deviation slightly increases again after the initial decrease (Fig. 4b). This is caused by a slight structure

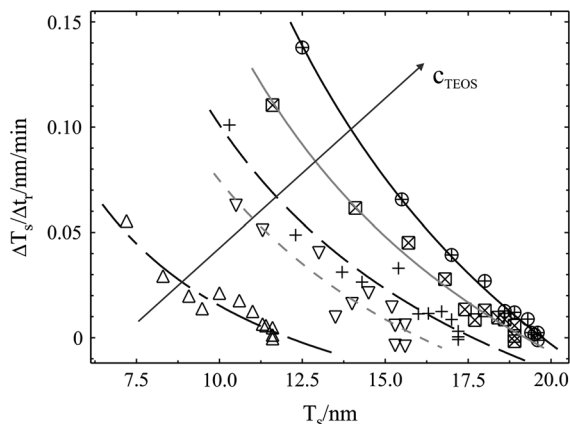


**Fig. 3** The growth rate  $\Delta T_s/\Delta t_r$  versus the corresponding shell thickness  $T_s$  at variable  $c_{\text{TEOS}}$  corresponding to Fig. 2a, approximated by  $\Delta r/\Delta t \sim A(r^{-1} + B)$  (lined curves) described by Sugimoto (1987) for the case of diffusion-limited growth kinetics of first order in monomer concentration

loss in the scattering curves. As shown by TEM micrographs in Fig. 2c, the products synthesized at high  $c_{\text{TEOS}}$  (0.043 mol/L and 0.052 mol/L) show additional tiny silica particles, which may be formed by homogeneous nucleation. As a consequence, the measured intensity is composed of the scattering by both the composites and the tiny silica particles, resulting in slight smearing of the detected side maximum.

By definition, the standard deviation determined by Eq. 4 only provides information on the polydispersity of the shell thickness. However, it is of crucial importance to consider that the scattering curves may additionally be affected by many other factors, e.g., irregular geometry, superimposed scattering by pure silica particles, density fluctuations, desmearing artefacts, etc. Consequently, the measured standard deviation of the shell thickness during the coating process might be used for on-line monitoring of the product homogeneity.

#### Variation of ammonia concentration and reaction temperature

The results discussed above show that  $\text{Fe}_3\text{O}_4$  particles can be coated with a compact silica shell of the desired thickness by varying the precursor concentration. Furthermore, it is known that ammonia plays an important role in the coating process based on the

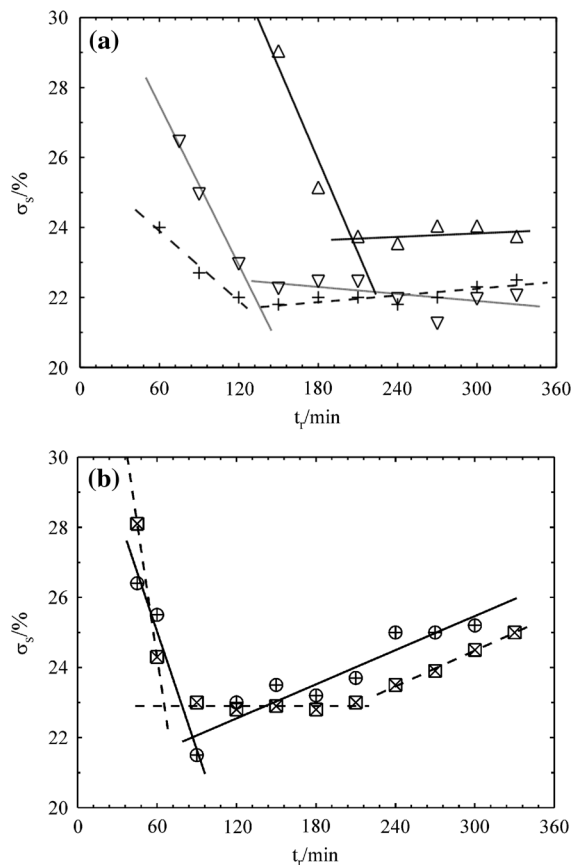


**Fig. 4** The standard deviation  $\sigma_s$  measured by SAXS versus the reaction time  $t_r$  for **a**  $c_{\text{TEOS}} = 0.017$  mol/L (white up-pointing triangle),  $c_{\text{TEOS}} = 0.026$  mol/L (white down-pointing triangle),  $c_{\text{TEOS}} = 0.035$  mol/L (plus), and **b**  $c_{\text{TEOS}} = 0.043$  mol/L (squared times),  $c_{\text{TEOS}} = 0.052$  mol/L (circled plus)

classic Stöber reaction. On the one hand, investigations by Deng et al. (2005) revealed that a critical ammonia concentration must not be exceeded. Otherwise, homogeneous nucleation may occur, i.e., pure silica would be produced. On the other hand, it is known from the classic Stöber reaction that the condensation rate is affected more strongly by  $c_{\text{NH}_3}$  as compared to the hydrolysis rate. A low  $c_{\text{NH}_3}$  therefore favors the production of hydrolyzed intermediates. In addition, the lower  $c_{\text{NH}_3}$  is adjusted, the lower is the colloidal stability of the suspension. As a result, the hydrolyzed intermediates tend to aggregate. Consequently, gelation may occur, if  $c_{\text{NH}_3}$  is adjusted below a critical minimum. As it acts as a catalyst and colloidal stabilizer,  $c_{\text{NH}_3}$  must therefore be adjusted within an appropriate range.



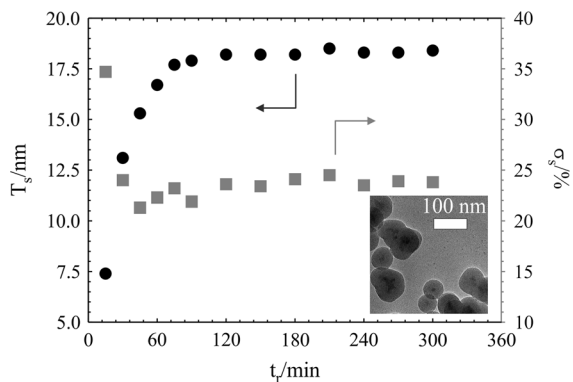


**Fig. 5** The shell thickness  $T_s$  (black circle) and standard deviation  $\sigma_s$  (grey square) plotted versus the reaction time  $t_r$  for  $c_{\text{NH}_3} = 0.39$  mol/L and the TEM micrograph of the final product (inset)

The syntheses discussed above were conducted at  $c_{\text{NH}_3} = 0.13$  mol/L. To study the influence of ammonia, two additional syntheses were conducted at a low  $c_{\text{NH}_3}$  (0.06 mol/L, T035N06-20, Table 1) and high  $c_{\text{NH}_3}$  (0.39 mol/L, T035N39-20). The TEOS concentration was kept constant at  $c_{\text{TEOS}} = 0.035$  mol/L. Figure 5 displays the  $T_s$  (black circle) and  $\sigma_s$  (grey square) as a function of  $t_r$  as obtained from SAXS measurements for  $c_{\text{NH}_3} = 0.39$  mol/L. Obviously, the time evolution of  $T_s$  and  $\sigma_s$  shows analogous characteristics to those obtained for the above synthesis at  $c_{\text{NH}_3} = 0.13$  mol/L (plus, Figs. 2a, 4a). The obtained parameters differ only slightly ( $T_s = 17.5 \rightarrow 18.5$  nm,  $\sigma_s = 22 \rightarrow 24$  %). From the inset of Fig. 5, it is obvious that the composites were produced successfully under these reaction conditions, i.e., the critical upper limit of  $c_{\text{NH}_3}$  has not been reached. However, it is evident that the growth rate increased significantly as  $c_{\text{NH}_3}$  increased from 0.13 to 0.39 mol/L.

After the decrease of  $c_{\text{NH}_3}$  from 0.13 to 0.06 mol/L, the measured SAXS curves differ (Fig. 6) from the scattering curves exemplarily as shown in Fig. 1a. While the intensity increases slightly with  $t_r$ , a side maximum could not be observed in the profiles. As shown by the TEM micrograph in the inset of Fig. 6, aggregates of pure silica were formed. Obviously,  $c_{\text{NH}_3}$  was adjusted below a critical minimum and silica gelation occurred (sol-gel transition). The “product inhomogeneity” achieved is clearly reflected by the SAXS curves, since the profiles do not exhibit any shell-related side maxima.

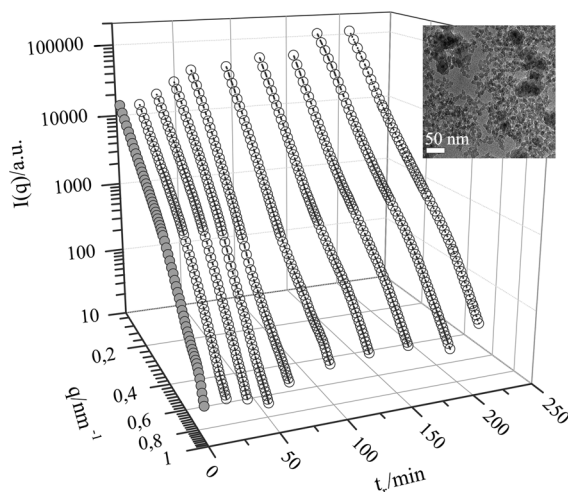


**Fig. 6** Measured scattering curves  $I(q)$  versus reaction time  $t_r$  for  $c_{\text{NH}_3} = 0.06$  mol/L and the TEM micrograph of final product (inset)

To study the effect of the reaction temperature  $T_r$ , coating was conducted at an elevated temperature of  $T_r = 40$  °C. The initial reaction conditions are listed in Table 1 (synthesis T043N13-40). The corresponding coating experiment conducted at 20 °C has already been discussed above (synthesis T043N13-20, Table 1). In case of  $T_r = 40$  °C, the scattering profiles exhibit an analogous behavior at the beginning of the reaction, i.e., a shell-related side maximum was reached (Fig. 7a). With increasing  $t_r$ , however, the side maximum became less visible and vanished almost completely at the end of the coating process. The core-shell sphere model (Eq. 4) was fitted to the curves (Fig. 7a, solid lines), and the resulting  $T_s$  and  $\sigma_s$  are depicted in Fig. 7b. Obviously, the shell thickness gradually increases with increasing reaction time, up to a final size of about 1.7 nm. As a result of the structure loss of scattering curves, the standard deviation does not decrease but increases from about 30 up to 47 %. As mentioned above, the structure loss of the scattering curves may be caused by several factors. As evident from the TEM micrographs (inset of Fig. 7b), the structure loss in the scattering profile here is caused by the superimposed scattering of pure silica particles formed parallel to the coating reaction. Obviously, homogeneous nucleation is favored at 40 °C, resulting in the formation of stable Stöber particles.

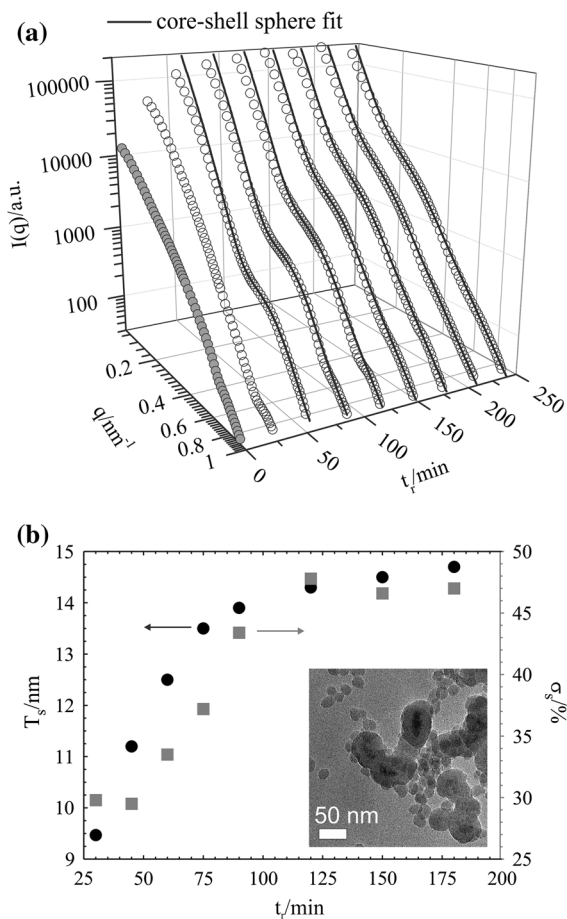


**Fig. 7** **a** Scattering curves  $I(q)$  measured at an elevated reaction temperature of 40 °C; **b** the resulting shell thickness and standard deviation plotted versus reaction time  $t_r$  and TEM micrograph of the final product (*inset*)

## Summary and conclusion

Many papers deal with the production of  $\text{Fe}_3\text{O}_4@\text{SiO}_2$ . Often, conclusions have been drawn with respect to the influence on the final shell thickness from using indirect characterization methods, e.g., vibrating sample magnetometer, XRD, UV–Vis spectroscopy, etc. Normally, TEM analyses are used for the qualitative estimation of the resulting shell thickness under various reaction conditions. To the best of our knowledge, however, quantitative studies of shell growth *dynamics*, i.e., investigations of its time evolution during progressing coating reaction still remain to be performed. The goal of this paper was to demonstrate the potential of our laboratory-scale SAXS instrument for such quantitative investigations.

To this end,  $\text{Fe}_3\text{O}_4@\text{SiO}_2$  composites were synthesized under various conditions, and the time-resolved SAXS measurements were conducted. The measured intensity profiles were fitted using the ideal core–shell sphere model. As the  $\text{Fe}_3\text{O}_4$  particles were synthesized by co-precipitation, high polydispersity and irregular particle shapes resulted. Interestingly, SAXS provided reliable information on the shell thickness that was in very good agreement with TEM observations despite the complex geometry of the synthesized nanocomposites. Apart from the time-resolved acquisition of data, the SAXS method also offers a high potential for on-line monitoring of the shell growth using the SAXS camera.

By means of time-resolved SAXS measurements and TEM observations, the effect of the initial TEOS concentration on the shell growth kinetics was studied. To this end,  $\text{Fe}_3\text{O}_4$  particles were coated by the classic Stöber method, and the time-dependent SAXS data were fitted by the core–shell sphere model. The resulting shell thickness as a function of the reaction time at variable TEOS concentrations was determined well by our SAXS device. Under the given reaction conditions, the shell growth kinetics was found to be affected in such a way that the growth rate increased with increasing TEOS concentration. The time dependence of the shell thickness can be described by diffusion-limited growth kinetics of first order in precursor concentration. The decreasing standard deviation in the early reaction stage, indicating a self-sharpening shell growth mechanism, supports these conclusions. In contrast to its definition, however, the standard deviation of the shell thickness measured by SAXS may also be affected by many other factors, e.g., non-isometric shape and co-existing pure silica. As obvious from TEM micrographs for high TEOS concentrations, the initial morphology was developed from highly branched clusters at the beginning to unbranched and more isometric core–shell composites at the end of the reaction. Hence, the decrease of the measured standard deviation may be caused by both decreasing polydispersity and approaching isometric geometry.

Further experiments were conducted at high and low ammonia concentration, respectively. High ammonia concentration led to faster growth kinetics without any significant effect on the composite properties. At a low ammonia concentration, homogeneous nucleation was induced, followed by gelation.

As a consequence, the typical shell-related side maximum was not observed in the profile, which reflected the existing inhomogeneity (silica aggregates). Furthermore, an “unstable” coating process was achieved at an elevated reaction temperature. At the beginning of the reaction, the SAXS profiles showed the shell-related side maximum typical for low polydispersity. With increasing reaction time, the side maximum became less pronounced and vanished completely at the end of the reaction. Consequently, the resulting standard deviation gradually increased with increasing coating time. As shown by TEM micrographs, the structure loss can be related to homogeneous Stöber silica particles produced parallel to the coating process due to the fast kinetics at elevated temperature.

In conclusion, this work demonstrates how information on coating dynamics can be obtained using a laboratory SAXS instrument. Time dependence of the shell thickness can be determined well during the coating process. On this basis, growth kinetics can be derived under various reaction conditions. Furthermore, SAXS curves provide additional information on product homogeneity by considering the shell-related side maximum in the measured profiles. In the future, SAXS might be applied for the in situ investigation of properties of continuously synthesized particles. When equipped with a fast read-out detector, the self-developed SAXS instrument is highly useful for the quantitative determination of particle-related parameters for the efficient on-line monitoring of product properties.

**Acknowledgments** The research work producing these results was funded by the German Research Foundation (DFG Ni 414/13-1). We also acknowledge the support by the European Union’s Seventh Framework Programme under Grant Agreement No. 280765 (BUONAPART-E).

## References

- Beaucage G (1996) Small-angle scattering from polymeric mass fractals of arbitrary mass-fractal dimension. *J Appl Crystallogr* 29:134–146. doi:10.1107/s0021889895011605
- Boukari H, Lin JS, Harris MT (1997a) Probing the dynamics of the silica nanostructure formation and growth by SAXS. *Chem Mater* 9(11):2376–2384. doi:10.1021/cm9702878
- Boukari H, Lin JS, Harris MT (1997b) Small-angle X-ray scattering study of the formation of colloidal silica particles from alkoxides: primary particles or not? *J Colloid Interface Sci* 194(2):311–318. doi:10.1006/jcis.1997.5112
- Bruce IJ, Taylor J, Todd M, Davies MJ, Borioni E, Sangregorio C, Sen T (2004) Synthesis, characterisation and application of silica-magnetite nanocomposites. *J Magn Magn Mater* 284:145–160. doi:10.1016/j.jmmm.2004.06.032
- Caruana L, Costa AL, Cassani MC, Rampazzo E, Prodi L, Zaccheroni N (2012) Tailored SiO<sub>2</sub>-based coatings for dye doped superparamagnetic nanocomposites. *Colloid Surf A* 410:111–118. doi:10.1016/j.colsurfa.2012.06.027
- Chen ZH, Hwang SH, Zeng X-b, Roh J, Jang J, Ungar G (2013) SAXS characterization of polymer-embedded hollow nanoparticles and of their shell porosity. *J Appl Crystallogr* 46:1654–1664. doi:10.1107/s0021889813025132
- Debye P (1915) Zerstreuung von Röntgenstrahlen. *Ann Phys* 46:809
- Deng YH, Wang CC, Hu JH, Yang WL, Fu SK (2005) Investigation of formation of silica-coated magnetite nanoparticles via sol-gel approach. *Colloid Surf A* 262(1–3):87–93. doi:10.1016/j.colsurfa.2005.04.009
- Ding HL, Zhang YX, Wang S, Xu JM, Xu SC, Li GH (2012) Fe<sub>3</sub>O<sub>4</sub>@SiO<sub>2</sub> core/shell nanoparticles: the silica coating regulations with a single core for different core sizes and shell thicknesses. *Chem Mater* 24(23):4572–4580. doi:10.1021/cm302828d
- Elingarami S, Zeng X (2011) A short review on current use of magnetic nanoparticles for bio-separation, sequencing, diagnosis and drug delivery. *Adv Sci Lett* 4(11–12):3295–3300. doi:10.1166/asl.2011.1884
- Glatter O, Kratky O (1982) Small angle X-ray scattering. Academic, London
- Goertz V, Dingenouts N, Nirschl H (2009) Comparison of nanometric particle size distributions as determined by SAXS, TEM and analytical ultracentrifuge. *Part Part Syst Charact* 26(1-2):17–24. doi:10.1002/ppsc.200800002
- Goertz V, Gutsche A, Dingenouts N, Nirschl H (2012) Small-angle X-ray scattering study of the formation of colloidal SiO<sub>2</sub> Stober multiplets. *J Phys Chem C* 116(51):26938–26946. doi:10.1021/jp3111875
- Gregory AP, Clarke RN, Cox MG (2009) Traceable measurement of dielectric reference liquids over the temperature interval 10–50 °C using coaxial-line methods. *Meas Sci Technol* 20(7):075106. doi:10.1088/0957-0233/20/7/075106
- Guinier A, Fournet G (1955) Small-angle scattering of X-rays. Wiley, New York
- Guo X, Gutsche A, Nirschl H (2013a) SWAXS investigations on diffuse boundary nanostructures of metallic nanoparticles synthesized by electrical discharges. *J Nanopart Res* 15(11):1–13. doi:10.1007/s11051-013-2058-7
- Guo X, Gutsche A, Wagner M, Seipenbusch M, Nirschl H (2013b) Simultaneous SWAXS study of metallic and oxide nanostructured particles. *J Nanopart Res* 15(4):1–3. doi:10.1007/s11051-013-1559-8
- Hasany SF, Abdurahman NH, Sunarti AR, Jose R (2013) Magnetic iron oxide nanoparticles: chemical synthesis and applications review. *Curr Nanosci* 9(5):561–575
- Jeong U, Teng X, Wang Y, Yang H, Xia Y (2007) Superparamagnetic colloids: controlled synthesis and niche applications. *Adv Mater* 19(1):33–60. doi:10.1002/adma.200600674

- Liu B, Wang D-P, Huang W-H, Yao A-H, Koji I (2008) Preparation of core-shell  $\text{SiO}_2/\text{Fe}_3\text{O}_4$  nanocomposite particles via sol-gel approach. *J Inorg Mater* 23(1):33–38
- Massart R (1981) Preparation of aqueous magnetic liquids in alkaline and acidic media. *IEEE Trans Magn* 17(2):1247–1248. doi:10.1109/tmag.1981.1061188
- Mine E, Yamada A, Kobayashi Y, Konno M, Liz-Marzan LM (2003) Direct coating of gold nanoparticles with silica by a seeded polymerization technique. *J Colloid Interface Sci* 264(2):385–390. doi:10.1016/s0021-9797(03)00422-3
- Philipse AP, Vanbruggen MPB, Pathmamanoharan C (1994) Magnetic silica dispersions—preparation and stability of surface-modified silica particles with a magnetic core. *Langmuir* 10(1):92–99. doi:10.1021/la00013a014
- Pontoni D, Narayanan T, Rennie AR (2002) Time-resolved SAXS study of nucleation and growth of silica colloids. *Langmuir* 18(1):56–59. doi:10.1021/la015503c
- Roshan Deen G, Oliveira CLP, Pedersen JS (2009) Phase behavior and kinetics of phase separation of a nonionic microemulsion of C12E5/water/1-chlorotetradecane upon a temperature quench. *J Phys Chem B* 113(20):7138–7146. doi:10.1021/jp808268m
- Safarik I, Safarikova M (2002) Magnetic nanoparticles and biosciences. *Monatsh Chem* 133(6):737–759. doi:10.1007/s007060200047
- Shinkai M (2002) Functional magnetic particles for medical application. *J Biosci Bioeng* 94(6):606–613. doi:10.1016/s1389-1723(02)80202-x
- Stöber W, Fink A, Bohn E (1968) Controlled growth of monodispersed silica spheres in micron size range. *J Colloid Interface Sci* 26(1):62. doi:10.1016/0021-9797(68)90272-5
- Sugimoto T (1987) Preparation of monodispersed colloidal particles. *Adv Colloid Interface Sci* 28(1):65–108. doi:10.1016/0001-8686(87)80009-x
- Tobler DJ, Benning LG (2013) In situ and time resolved nucleation and growth of silica nanoparticles forming under simulated geothermal conditions. *Geochim Cosmochim Acta* 114:156–168. doi:10.1016/j.gca.2013.03.045
- Wengeler R, Wolf F, Dingenouts N, Nirschl H (2007) Characterizing dispersion and fragmentation of fractal, pyrogenic silica nanoagglomerates by small-angle X-ray scattering. *Langmuir* 23(8):4148–4154. doi:10.1021/la063073q
- Zhang X-l, Niu H-y, Li W-h, Shi Y-l, Cai Y-q (2011) A core-shell magnetic mesoporous silica sorbent for organic targets with high extraction performance and anti-interference ability. *Chem Commun* 47(15):4454–4456. doi:10.1039/c1cc10300h